Chapter 15

Heat Transfer Enhancement of Impinging Jet by Notched – Orifice Nozzle

Toshihiko Shakouchi and Mizuki Kito

Additional information is available at the end of the chapter

http://dx.doi.org/10.5772/52029

1. Introduction

Jets are one of the most interesting and widely applied phenomena because they exhibit free or wall-bounded shear turbulent flows and large vortex structures that are essential in fluid dynamics and engineering. Jets are used for various industrial applications such as jet and rocket propulsion, cleaning, cutting, heating, cooling, atomizing, and burning (Shakouchi, 2004). Numerous studies have focused on gaining an understanding of free jets because this is essential for improving their heat transfer performance. For example, Livingood & Hrycak (1973), Hrycak (1981), Downs & James (1987), and Viskanta (1993) presented literature surveys of the impingement heat transfer of jets. Martin (1977) examined heat and mass transfer for single round nozzle, single slot nozzle, arrays of round and slot nozzles and provided extended reviews of heat transfer data. Yokobori et al. (1978) showed the role of large-scale eddy structures in the heat transfer enhancement of impinging slot jets. They also demonstrated that the present of a small disturbance in the upstream free shear layer enhanced the heat transfer in the stagnation region. Kataoka et al. (1987) showed the effects of surface renewal by large-scale eddies on the heat transfer of impinging jets. They explained that a secondary peak heat transfer occurs because of intermittent motions which entrain ambient fluid and break up the thermal boundary layer on the wall. Antonia & Zhao (2001) examined two circular jets—a pipe jet with a fully developed turbulent flow profile and a contraction jet with a laminar top-hat velocity profile at the nozzle exit—and discussed the similarities and differences between the two. Quinn (2006) demonstrated the effects of nozzle configurations on the mixing characteristics from the mean velocity and pressure distributions of an orifice plate and contoured nozzle jets. Mi et al. (2001) investigated the mixing characteristics and physical mechanisms of jets issuing from an orifice plate using flow visualization images and temperature measurements in comparison with a contoured nozzle and a pipe and found that the mixing rate of the orifice plate jet was higher than that of the others.

Impinging jets are applied in a wide variety of rapid cooling and heating processes because of their high efficiency and ability to provide high heat transfer rates. Many experiments and numerical simulations have been carried out to reveal the mechanism of impinging jets and to improve their performance. The effects of nozzle configurations, jet velocity, and exit conditions have been well recognized. Viskanta (1993) presented detailed reviews of the impingement heat transfer of single round and slot jets, a row of round and slot jets, inline and staggered arrays of round jets, square arrays of slot jets, a single row of round jets with cross flow, inline and staggered arrays of round jets with cross flow of spent air, an obliquely impinging single round jet, a slot jet with cross flow (jet inclined against cross flow), and a single round or slot jet impinging on concave and convex surfaces. He also discussed the impingement heat transfer of single flame jets and flame jet arrays.

Orifice jets are well known for their interesting characteristics—such as the vena contracta effect—and for having high mixing performance and good heat transfer characteristics; however, only a few studies have focused on these issues. Lee, J. & Lee, SJ. (2000) used three different orifice nozzles—square-, standard-, and sharp-edged—and demonstrated that the edge configuration of orifice nozzles affects the heat transfer characteristics of jet impingement. Quinn (2006) also demonstrated the effects of nozzle configurations on the mixing characteristics by measuring the mean velocity and pressure distributions for orifice and contoured-nozzle jets. Zhou et al. (2006) investigated the flow structure and the heat transfer characteristics of an orifice impinging jet with various mesh screens installed inside the nozzle. They also demonstrated the influence of the Reynolds number, nozzle-plate distance, and screen location on the heat transfer enhancement.

However, these studies have not provided an adequately detailed understanding of orifice jets. Therefore, this chapter provides an introduction to orifice jets and notched-orifice jets. This chapter has six sections. Sections 3 and 4 discuss orifice jets. Specifically, it describes the general characteristics of an orifice jet in comparison with a pipe and a quadrant jet, including the effects of the nozzle contraction area ratio on the free and heat transfer characteristics. Section 5 discusses the proposed notched-orifice jet. Specifically, it discusses the characteristics of a notched-orifice nozzle that is conically tapered on the inside to reduce the flow resistance and simultaneously increase the turbulent intensity.

2. Orifice jets

Before presenting a detailed analysis of orifice jets, we discuss their general characteristics in this section.

Figure 1 shows a pipe nozzle having an orifice nozzle with a 10-mm exit diameter and a pipe with a 29.75-mm inner diameter and a quadrant nozzle that provides a uniform velocity profile at the nozzle exit, which can be regarded as the standard profile for fundamental numerical and experimental studies. The quadrant nozzle contracted from a diameter of 29.75 mm to the exit diameter of 10.0 mm, which smoothly connected to a 3.0-mm-long straight contour [see Fig. 1 (c)]. Every nozzle had an exit diameter d_o = 10.0 mm,

thickness of 1.0 mm, and length of 500 mm to ensure a fully developed turbulent pipe flow at the nozzle exit. Note that all the jets issued from a pipe having an exit velocity profile matching that of a fully developed turbulent pipe flow even in the case of a pipe with an inner diameter d_i = 29.75 mm, for which the pipe length ratio L/d_i = 16.8.

2.1. Nozzle exit characteristics

A constant temperature hot-wire anemometer was used to measure the mean and fluctuating velocity for an air jet at Reynolds number $Re = 1.5 \times 10^4$, which is based on the nozzle exit diameter and jet exit velocity.

The mean exit velocity profiles at $Re = 1.5 \times 10^4$, which should be sufficiently higher to describe an incompressible flow, are shown in the left-hand side of Fig. 2, and the fluctuating velocity for each jet is shown on the right-hand side because it was axisymmetric. The x- and r-axes starting at the origin of the jet were taken in the streamwise and spanwise directions, respectively. In the cross-stream direction, the origin $r = 0$ was taken at the centerline of the jet.

In the case of the pipe jet, the mean velocity profile of the pipe jet matched a fully developed turbulent pipe flow because the 500-mm-long pipe is sufficiently long for the boundary layer to grow completely. The fluctuating velocity reflecting the steep velocity gradient near the center of the jet is higher than that of the orifice jet that is discharged toward the center of the jet and accelerated.

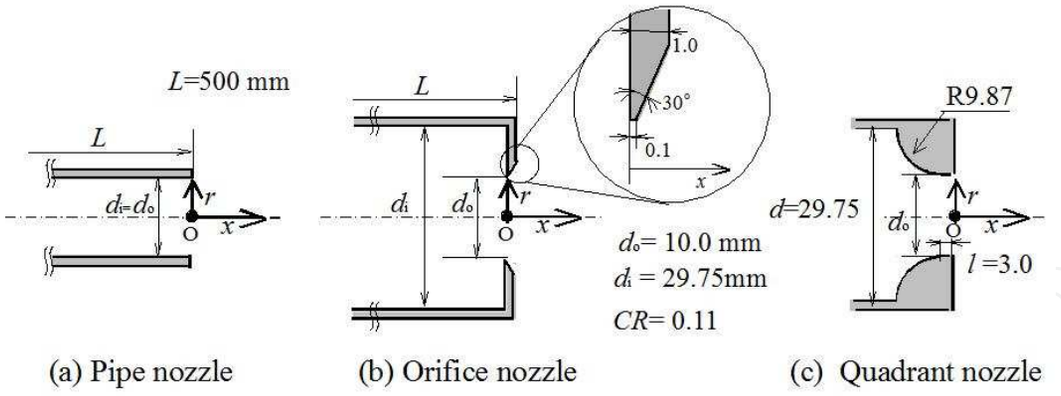

Figure 1. Nozzle configuration

The exit velocity of a quadrant nozzle also has a thin shear layer. However, the uniform velocity area over the nozzle exit is wider than that of the orifice jet because there is no vena contracta effect. It is therefore not surprising that the quadrant jet velocity u_c / u_m (u_m : mean velocity at the nozzle exit) is smaller than the others. The orifice jet velocity at the center is $u_c / u_m \cong 1.3$, and the quadrant jet velocity is approximately 15% smaller than the orifice jet velocity at the center. The maximum fluctuating velocities are observed at the largest velocity gradients.

On the other hand, the orifice jet has a considerable effect on the exit velocity profile. Jets issuing from an orifice nozzle are characterized by their large velocity gradient at the jet edge and the vena contracta effect, which decreases the jet diameter immediately after discharging and increases the centerline jet velocity, as shown in Fig. 3. The orifice jet has a saddle-shaped profile because of the vena contracta effect. The maximum fluctuating velocity of the orifice jet occurring at the jet edge is attributed to the exit velocity vector inside the nozzle toward the center because of the contraction of the orifice nozzle. Therefore, an orifice jet can potentially improve the mixing and spreading characteristics and the entrainment of ambient fluid.

However, it is true that the flow resistance of an orifice nozzle at the nozzle exit increases compared to that in a pipe and a quadrant nozzle. The flow resistance can be caused by the annular vortex inside the nozzle edge, as shown in Fig. 3. In order to avoid the increase in the flow resistance at the nozzle exit, a contour nozzle or a quadrant nozzle is commonly used. While the annular vortex causes a high flow resistance, it also increases the centerline velocity. The increase in the centerline velocity is one of major factors that enhance the heat transfer ratio on the impingement plate. There is no increase in the centerline velocity when the contour nozzle or quadrant nozzle is used because the jet produces a uniform flat velocity profile at the nozzle exit. In contrast, the orifice jet having a saddle-backed velocity profile because of the vena contracta effect appears to have a higher centerline velocity and enhances the heat transfer ratio. The detailed flow and heat transfer characteristics are presented in the following sections.

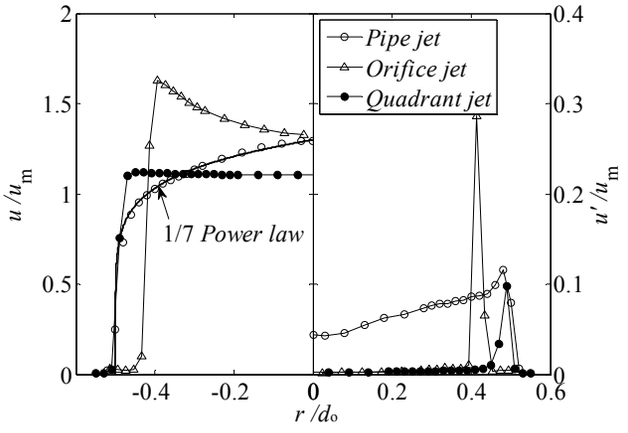

Figure 2. Mean and fluctuating velocities at the nozzle exit (x/d_o=0.2)

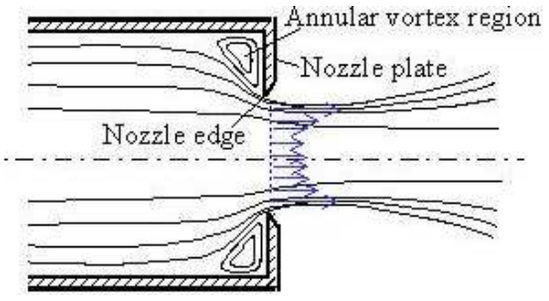

Figure 3. Orifice jet

2.2. Free flow jet characteristics

Figure 4 (a) and (b) show the normalized centerline velocity u_c/u_m and turbulent intensity u'_c/u_m for a pipe, an orifice, and a quadrant nozzle at $Re = 1.5 \times 10^4$. The orifice jet shows a different profile compared to the pipe and quadrant jets. The centerline velocity increases from the nozzle exit and reaches the maximum at $x/d_o \cong 2.0$ because of the vena contracta effect, whereas the velocity remains almost constant from the nozzle exit to $x/d_o \cong 4.0$ and 5.0 for the jet of the pipe nozzle and the quadrant nozzle, respectively. The velocity u_c/u_m decays according to the equation (1) in the fully developed region, which agrees with the equation for an axisymmetric circular jet.

$$u_c / u_m \propto \left(x / d_o\right)^{-1.0} \tag{1}$$

The turbulent intensity initially remained relatively small, following which it suddenly increased for all jets. The sudden increase occurs in the transition region in the case of the pipe jet. The quadrant jet shows the smallest turbulent intensity.

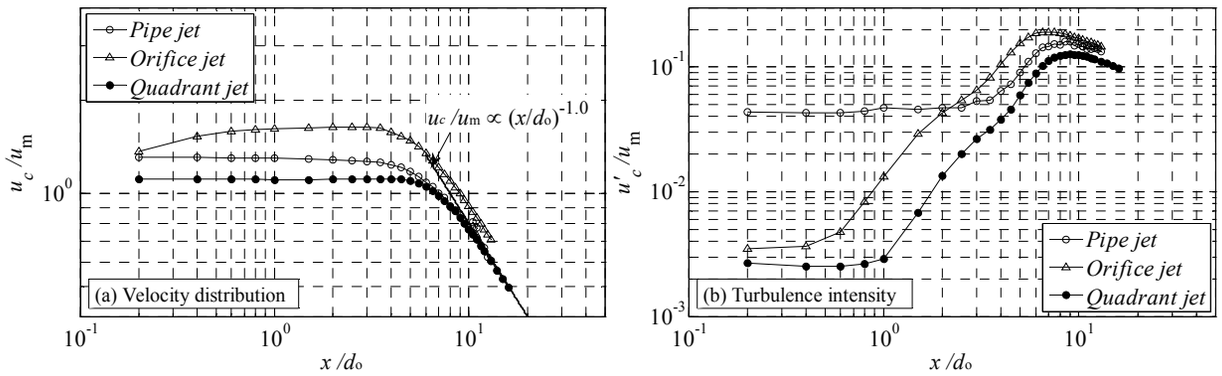

Figure 4. Mean and fluctuating velocity distributions along the jet centerline

2.3. Heat transfer characteristics

The local Nusselt number at $Re = 1.5 \times 10^4$ was calculated from the temperature distribution measured using thermocouples on the impinging plate and the jet temperature. The jet temperature was controlled carefully to within ±0.3°C of the atmospheric temperature. Thus, the entrainment effect claimed by Martin (1977) is neglected. To estimate the conduction heat flux, the heat loss due to radiation and natural convection were considered. The heat loss due to natural convection was estimated by measuring the temperature inside and on the surface of the impinging plate. The average Nusselt number is defined as the equation (2).

$$\overline{Nu} = \left(\frac{1}{\pi r^2}\right) \int_0^r Nu(2\pi r)dr \tag{2}$$

where r is an arbitrary location.

Figure 5 shows the local Nusselt number for $H/d_o = 2.0$ at $Re = 1.5 \times 10^4$. The thermocouples were mounted on the plate along the $\pm r$ axis to assure the center of impinging jet. The temperature distributions were axisymmetric. The only the half region of r is shown in Fig. 5. The Nusselt number changes considerably depending on the nozzle configurations, especially in the stagnation region. The orifice jet enhances the local Nusselt number significantly. For instance, it increases by 17% and 33% at the stagnation point as compared to those of the pipe and the quadrant jets, respectively. The reduction in the local Nusselt number for the quadrant jet is attributed to the exit velocity being measured to be ~15% smaller than that of the other jets.

Figure 6 shows the operation power W at $Re = 1.5 \times 10^4$. The operation power W was calculated by the equation (3).

$$W = Q(DP + ru_{pm}{}^2 / 2) \tag{3}$$

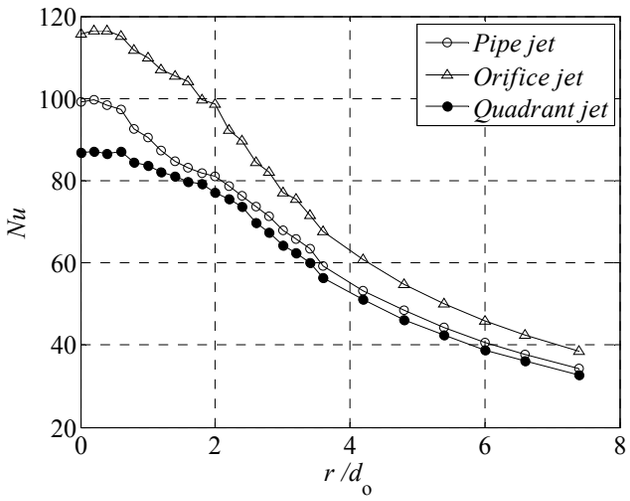

Figure 5. Local Nusselt number for $H/d_o = 2.0$ at $Re = 1.5 \times 10^4$

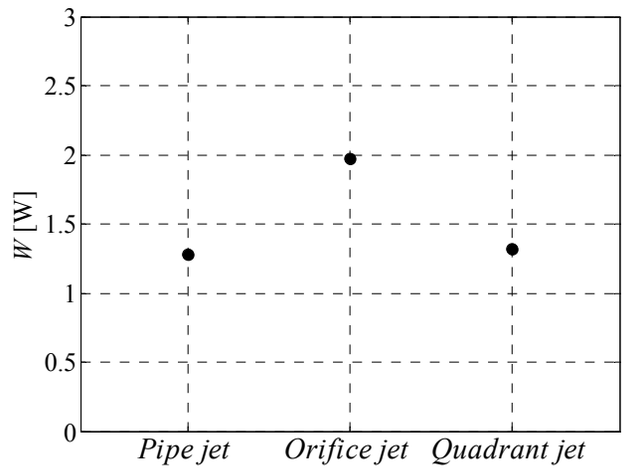

Figure 6. Operation power for the different nozzle types at Re=1.5×10⁴

where Q is the flow rate and ΔP, the pressure difference from atmospheric pressure. The static pressure was measured at $20d_o$ upstream from the nozzle exit using a 0.8-mm-diameter pressure tap mounted on the pipe nozzle wall at a flow rate of Q.

The required operation power of the orifice jet is larger than that of the pipe and the quadrant jets. As demonstrated above, the orifice jet provides better heat transfer performance because of the increase in its centerline velocity due to the vena contracta effect; however, it requires greater operation power because of its large flow resistance.

3. Flow control of orifice jet by changing nozzle contraction area ratio

Despite the evidence indicating that orifice jets improve the mixing and heat transfer characteristics, we were unable to find a systematic study of these jets that also focused on the nozzle contraction area ratio. Therefore, in this section, we consider the characteristics of orifice jets and the effects of nozzle configurations on their flow and heat characteristics by taking into account the nozzle contraction area ratio.

The nozzle geometry and the coordinate system are shown in Fig. 7 to reveal the effects of the nozzle contraction area ratio.

The contraction area ratio CR is defined as the equation (4).

$$CR = \left(\frac{A_o}{A_i} \right) = \left(\frac{d_o}{d_i} \right)^2 , \tag{4}$$

where A_o is the cross-sectional area of the nozzle exit; A_i, the cross-sectional area of the pipe; d_o, the exit diameter of the nozzle; and d_i, the inner diameter of the pipe. The contraction area ratio was varied from CR = 0.11 to 1.00 (pipe nozzle). The various CRs were obtained by changing the pipe diameter under a constant nozzle exit diameter of d_o = 10.0 mm.

3.1. Nozzle exit characteristics

The mean exit velocity profiles at $Re = 1.5 \times 10^4$ are plotted in the left-hand side of Fig. 8 and the fluctuating velocity for each CR is plotted on the right-hand side because it was axisymmetric. CR was found to have a considerable effect on the exit velocity profile. The mean velocity profile for CR = 1.00 (pipe jet) agrees with the fully developed turbulent pipe flow, as shown in Fig. 2. For CR = 0.69, the profile was nearly top-hat-shaped, and a stronger effect of contraction was observed as CR decreased. The orifice jets had saddle-shaped profiles due to the vena contracta effect and the smaller CR and they had a thinner shear layer. The orifice jet velocity at the centre was $u_c / u_m \cong 1.3$ for all the orifices. The smaller CR caused a smaller orifice jet width, reflecting the maximum velocity value. The maximum fluctuating velocities are observed at the largest velocity gradients. The value of the turbulent intensity at the jet centre decreased from 4.3% to 0.2% with decreasing CR.

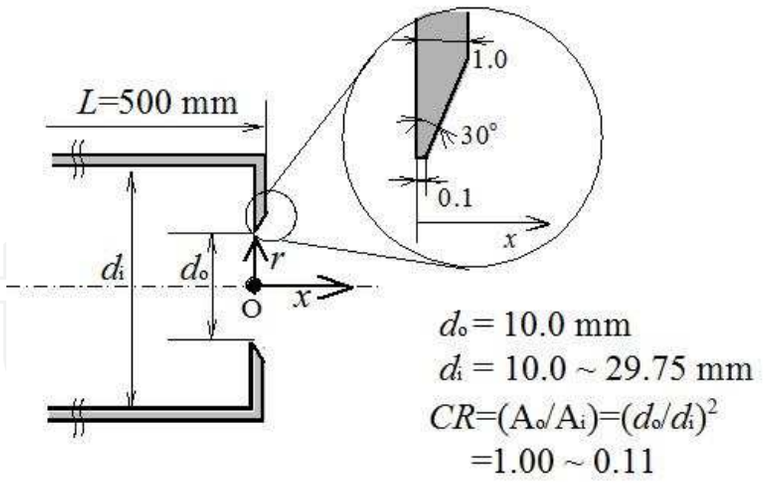

Figure 7. Nozzle configuration

3.2. Free flow jet characteristics

The centerline velocity u_c/u_m and turbulent intensity u'_c/u_m for various *CR* values at $Re = 1.5 \times 10^4$ are shown in Figs. 9(a) and (b), respectively. The centerline velocity increased from the nozzle exit and reached the maximum at $x/d_o = 2.0$ for all the orifice nozzles because of the vena contracta effect, whereas the velocity remained almost constant from the nozzle exit up to approximately $x/d_o = 4.0$ for the jet with $CR = 1.00$ (pipe nozzle).

The velocity growth from the exit increased with decreasing *CR*. The obtained turbulent intensity was apparently smaller at the exit and increased earlier as *CR* decreased. For example, for $CR = 0.11$, a sudden increase in turbulent intensity occurred at $x/d_o \cong 0.4$ and the maximum was at $x/d_o \cong 7.0$.

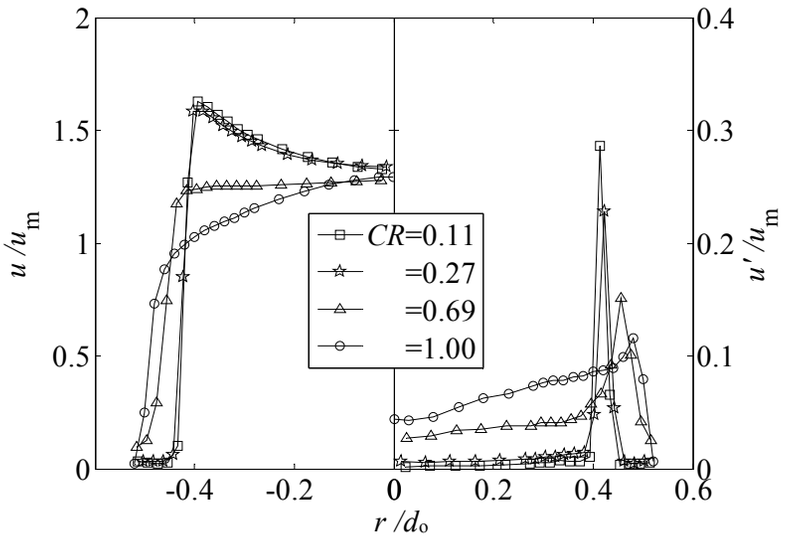

Figure 8. Mean and fluctuating velocities at the nozzle exit (x/d_o=0.2)

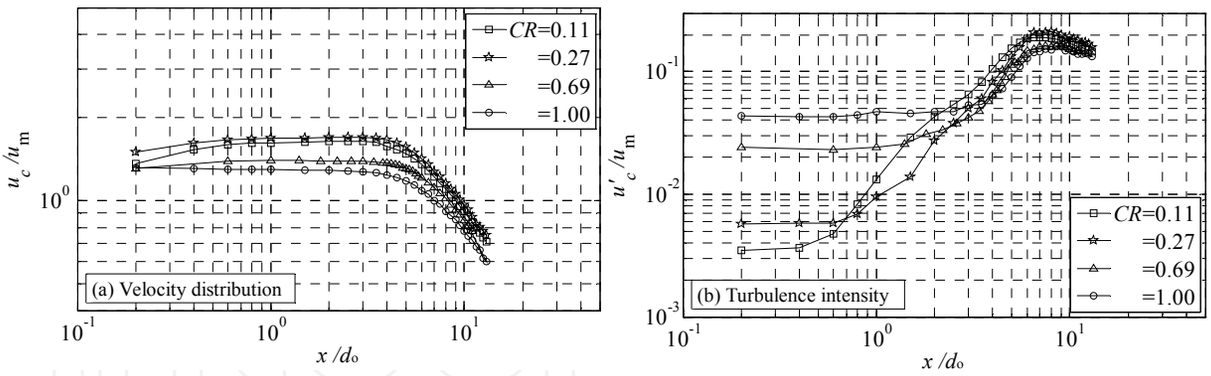

Figure 9. Mean and fluctuating velocity distributions along the jet centerline

The centerline maximum velocities for different values of *CR* at x/d_o = 2.0 are shown in Fig. 10. The centerline maximum velocity u_c/u_m can be expressed as follows:

$$u_c / u_m = 1.9CR^3 - 3.55CR^2 + 1.38CR + 1.53 \quad (5)$$

which has a maximum value of 1.7 at *CR* = 0.27. Velocity vectors towards the centerline produced by strong contraction at the orifice nozzle exit contributed to the increase in the centerline velocity, which had a maximum at *CR* = 0.27.

In order to obtain the dominant frequency of jet fluctuation where the jet reached its maximum velocity at x/d_o = 2.0, the power spectra were calculated from the velocity fluctuations at the jet center, as plotted in Fig. 11. The power spectra were normalized by integrating the function Φ_u^* as follows:

$\int \Phi_u^*(f^*)df^* = 1$, as proposed by Mi et al. (2001) for a comparison. The peak frequencies obtained for orifice jets at *CR* = 0.11, 0.27, 0.69, and 1.00 (pipe nozzle) and a quadrant nozzle were f^* = 0.71, 0.48, 0.55, 0.39, and 0.39, respectively, although the peak was not clear for *CR* = 1.00 (pipe nozzle). The values for the quadrant nozzle and *CR* = 0.11 are consistent with those reported by Mi et al. (2001). They presented values of $f^* \approx 0.40$ for a contoured nozzle and $f^* \approx 0.70$ for an orifice. Clearly, the peak frequency decreases with increasing *CR*. In addition, the magnitude of Φ_u^* at the peak also decreases and the peak becomes obscure, reflecting the large coherent vortex disintegrations. These results suggest that the same coherent vortex structures seen in Fig. 12 at low *Re* might exist at high *Re* as well.

The vortex structures of the submerged orifice water jet were visualized by the tracer method and the effects of *CR* on them were examined at low Reynolds number. Water jets seeded homogenously with Uranine (fluorescein) issued from the nozzle into a sufficiently large water tank. The images of the vortex structures were recorded using a digital video camera by illuminating the flow in the middle plane.

The results are shown in Fig. 12 for different *CR* values at $Re = 1.0 \times 10^3$. All of the flows were initially laminar and eventually became turbulent following the transition process.

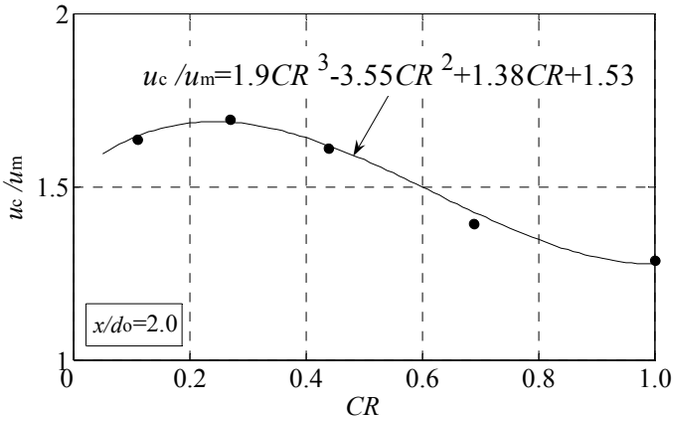

Figure 10. Centerline maximum velocity (x/d_o =2.0)

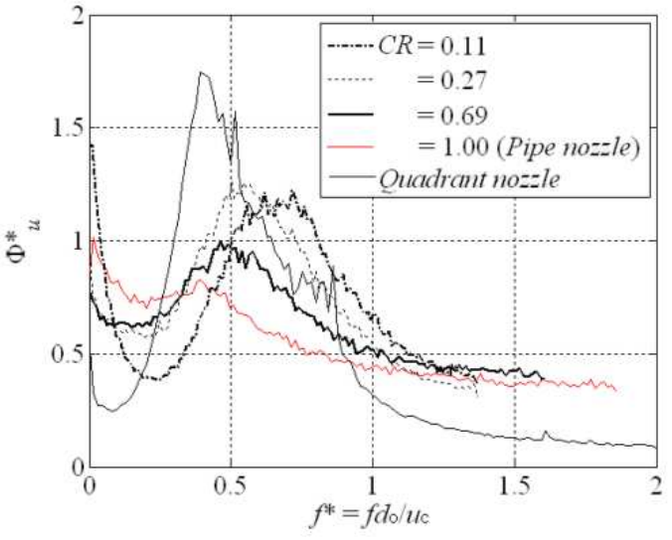

Figure 11. Power spectra at x/d_o =2.0.

Considerably large coherent vortexes were observed in Fig. 12 (a)–(b) and (d). Detailed observations of videos of the orifices jets revealed the production process of the large vortices. At first, many vortex rings were produced at the nozzle exit because of instability at the edge. A rapid decay in velocity in the downstream region prevented the formation of vortex rings, which yielded a large coherent vortex structure. *CR* caused significant changes in the formation of vortices. These changes must be related to the development of shear layer instability at the exit. Coherent vortex rings are observed in Fig. 12 (a) and (b), although those in Fig. 12 (b) are not as clear as those in the other cases. The coherent vortex rings produced for *CR* = 0.69 vanished in the downstream region. However, those produced for *CR* = 0.11 became incoherent in the downstream region, which promoted mixing with the ambient fluid. The mean velocity for *CR* = 0.11 increased and decreased more quickly than that for *CR* = 0.69, as explained in the next section. This may be the reason for the difference in the vortex formation. In contrast, there is no clear vortex in the pipe flow shown in Fig. 12 (c), suggesting the stability of the thick shear layer. It should be mentioned that even at $Re = 3.0 \times 10^3$, the flow was stable except in the most downstream region.

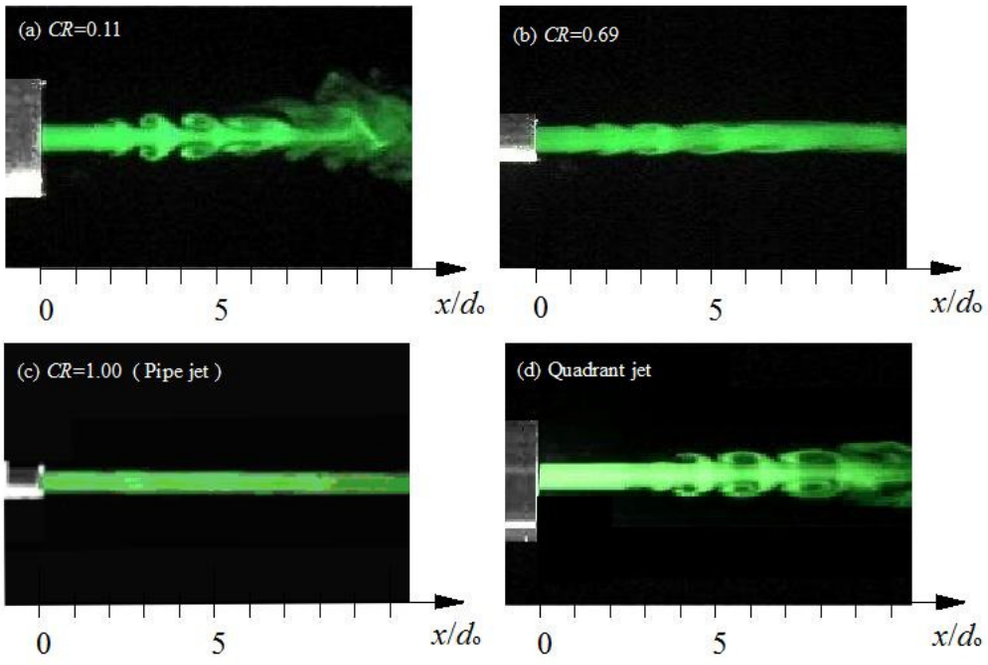

Figure 12. Flow visualization at Re=1.0×10^3

Figure 12 (d) also shows clear coherent vortexes produced by a quadrant nozzle because of instability at the edge of the nozzle exit, reflecting the thin shear layer shown in Fig. 8.

The large vortexes were stretched and appeared in the downstream region compared with the jet from the orifice nozzle that also had CR = 0.11, as shown in Fig. 12 (a). It is noteworthy that the jet from the quadrant nozzle did not grow as wide as those from the orifice nozzle. The flow for CR = 0.11 apparently spread wider and faster than the others at Re = 3.0 × 10^3 as well. Thus, the images indicate that the smaller CR enhances the mixing rate more and the velocity difference in the jet core region promotes the earlier merging of the coherent vortex.

3.3. Heat transfer characteristics

Figure 13 shows the local Nusselt number at H/d_o = 2.0 at Re = 1.5 × 10^4. The thermocouples were mounted on the plate along the r-axis on both sides in order to assure the center of impinging jet. The temperature distributed axisymmetrically after careful adjustment of the jet center. The distributions on only one side are shown in Fig. 13. The magnitude of the Nusselt number changed significantly with CR, especially at the stagnation point. The smaller CR enhanced the local Nusselt number significantly at Re = 1.5 × 10^4. The obtained heat transfer rates of orifice jets for CR = 0.11 and 0.27 were similar. In the case of CR = 0.11 and 0.27, the heat transfer rates were increased by 17% and 33% at the stagnation point compared to those of the pipe and the quadrant nozzle, respectively.

The effects of CR on the heat transfer characteristics of the impingement plate for a constant nozzle exit mean velocity u_m are shown in Fig. 13. The flow loss of the nozzle, however, increases with decreasing CR in practice. Therefore, the operation power W for constant u_m

increases for an orifice jet. In contrast, the centerline velocity u_c of the orifice jet increases as a result of the contraction effect (Fig. 10). If W is not larger and the increase in u_c is significant, we expect that the heat transfer characteristics of the orifice impinging jet will improve more than those of the pipe jet.

Here, we discuss the heat transfer characteristics on the impinging plate under the same operation power.

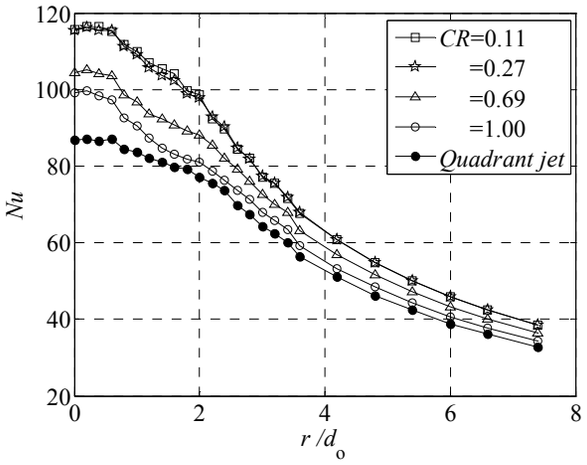

Figure 13. Local Nusselt number (H/d_o=2.0) at Re = 1.5 × 10⁴

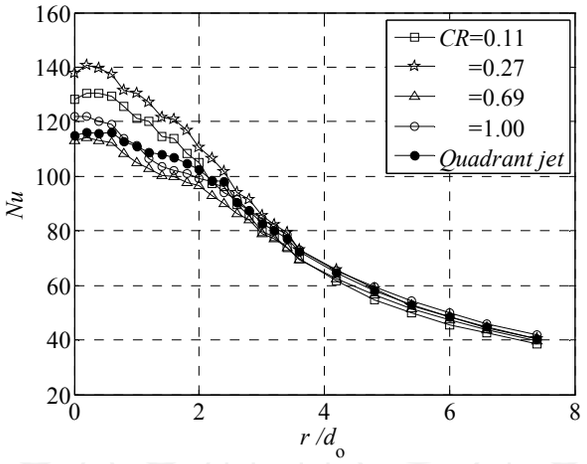

Figure 14. Local Nusselt number (H/d_o=2.0) under the same operation power

Figure 14 shows plots of the local Nusselt number distribution on the impingement plate for CR values ranging from 0.11 to 1.00 at H/d_o = 2.0 under the same operation power as that discussed in the previous section for CR = 0.11 (u_m = 22.9 m/s).

Because of the least flow loss from the nozzle, the nozzle exit mean velocity of the pipe jet was u_m = 30.4 m/s, which is larger than those of the orifice jets, under the same operation power as that required for CR = 0.11. However, because the orifice nozzle generates a contraction flow, the centerline velocity u_c increases from the nozzle exit and becomes maximum at H/d_o = 2.0. The maximum velocity ratio to u_m, u/u_m = 1.7, occurs for CR = 0.27.

An improved local Nusselt number is observed up to $r/d_o \cong 4$ for $CR = 0.27$ compared to that for the pipe. In addition, it should be noted that the local Nusselt number distribution for $CR = 0.11$ is smaller than that for the pipe. This is attributed to the large flow loss caused by the orifice nozzle for $CR = 0.11$.

4. Notched-orifice jet

We have seen the effects of the contraction area ratio $(d_o/d_i)^2$ on the flow characteristics of the orifice-free jets and the heat transfer enhancement in orifice impinging jets due to the increase in the centerline velocity that is caused by the vena contracta effect. However, it is found that the flow resistance of the orifice nozzle increases more than that of a nozzle without contraction. Reducing the flow resistance is essential for high performance. To reduce the flow resistance and improve the heat transfer characteristics using the vena contracta effect, we proposed a notched-orifice nozzle and demonstrated its flow and heat transfer characteristics.

In the previous section, the effects of the contraction area ratio of the orifice nozzle and operation power were discussed. These results suggest that the flow and heat transfer performances are governed by nozzle characteristics such as the jet impinging velocity, flow resistance, and turbulence intensity. Locating notches on the edge of the orifice nozzle exit will reduce the flow resistance and increase the turbulence intensity. Therefore, the heat transfer performance using the notched-orifice nozzle is expected to improve. The proposed nozzle geometry and coordinate system are shown in Fig. 15. Figure 15 (a) shows an orifice nozzle with a 10-mm exit diameter and a pipe with 19.23-mm inner diameter [$CR = (d_o/d_i)^2 = 0.27$]. Figure 15 (b) and (c) show V-shaped notched-orifice nozzles, namely, four- and eight-notched orifice nozzles, respectively. Four- or eight-notches having 60° openings and 1.56-mm depth are located on the edge of the orifice nozzle exit.

The nozzle exit diameter is generally selected as a reference length to represent the dynamical characteristics of jet flows. However, it is difficult to represent the universal dynamical characteristics for notched-orifice nozzles because there is little similarity in the flow patterns and characteristics even though the equivalent diameter based on the wet length and cross-sectional area is used. The investigations were performed considering the operation power calculated based on the flow resistance of each orifice jet under the same operation power as that of the orifice jet operated at $Re = 1.5 \times 10^4$.

4.1. Nozzle exit characteristics

Figure 16 shows the mean and fluctuating velocity distributions in the A-A′ and B-B′ directions at the nozzle exit $x/d_o = 0.2$ for the orifice, four-notched orifice, and eight-notched orifice jets. The mean exit velocity u/u_m is plotted in the left-hand side of Fig. 16 and the fluctuating velocity u'/u_m is plotted in the right-hand side because it is axisymmetric. A saddle-backed profile is observed for the orifice jet because of the vena contracta effect. The maximum fluctuating velocity of the orifice jet occurs at the jet edge attributed to the exit

velocity vector inside the nozzle toward the center because of the contraction of the orifice nozzle. A similar profile can be seen for the notched-orifice jets, especially in the B-B′ direction. The jet widths of the orifice jets increase because of the notches in the A-A′ plane, whereas the vena contracta effects appear in the B-B′ plane. The differences between the profiles in the A-A′ and B-B′ planes become less significant when the number of notches increases. This might be attributable to the interference of vortices produced by the notches. The fluctuating velocity of the notched-orifice jets increases in the A-A′ plane.

Figure 17 shows the flow rate Q at the nozzle exit under the same operation power. The flow rate Q of the notched-orifice jet increases while the flow resistance decreases more than that in the case of the orifice jet without notches because of the increase in the cross-sectional area at the nozzle exit. The flow rates Q of four- and eight-notched orifice jets increased by 9.7% and 10.9%, respectively, compared with that of the orifice jet.

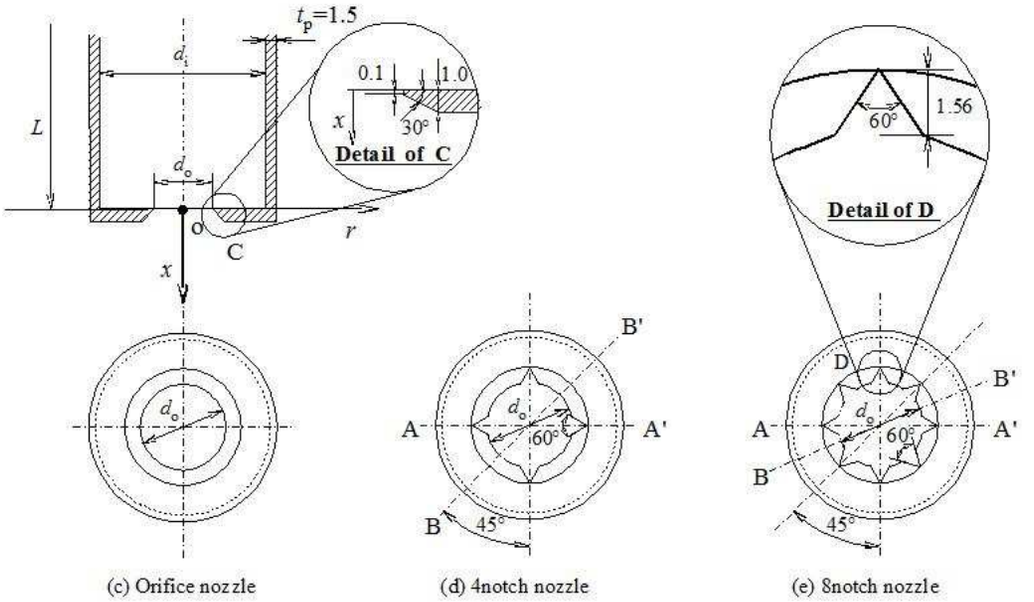

Figure 15. Nozzle configuration

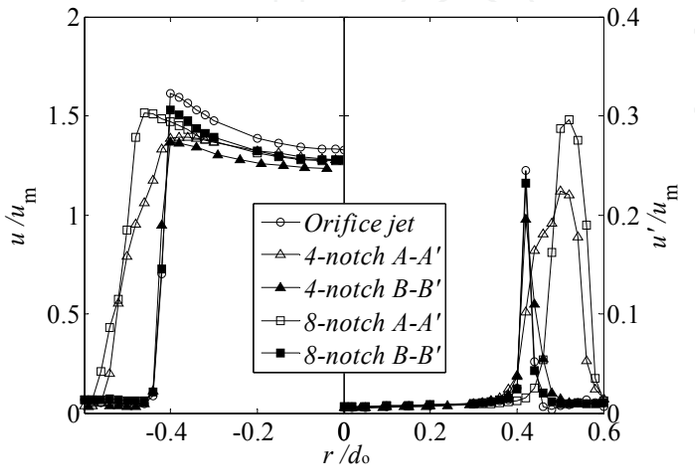

Figure 16. Mean and fluctuating velocities at the nozzle exit (x/d_o=0.2)

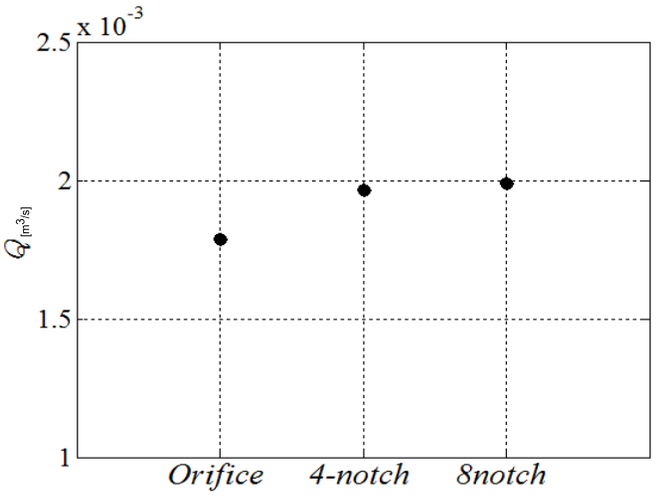

Figure 17. Flow rate at the nozzle exit

4.2. Free flow jet characteristics

The centerline velocity u_c and fluctuating velocity u_c' under the same operation power are plotted in Fig. 18. The centerline velocity increases from the nozzle exit for the orifice nozzles because of the vena contracta effect and remains nearly constant in a region called the potential core and then reaches the fully developed stage. Similar trends of development are also observed for the notched-orifice jets. In the case of a four-notched jet, the thick mixing layer reaches the center of the jet because of the significant difference between the velocity profiles in the A-A′ and B-B′ planes, as shown in Fig. 16, and causes the potential core length to be shorter than that of the other jets. The turbulence intensity along the jet centerline increases by ~47.2% at x/d_o = 3.5 compared with the other jets. In the case of the pipe jet, the turbulence intensity near the nozzle exit is larger than that of the other jets because the pipe jet had a fully developed turbulent velocity profile; however, the growth of the turbulence intensity is gradual and the turbulence intensity decreases at $x/d_o \geq 3$.

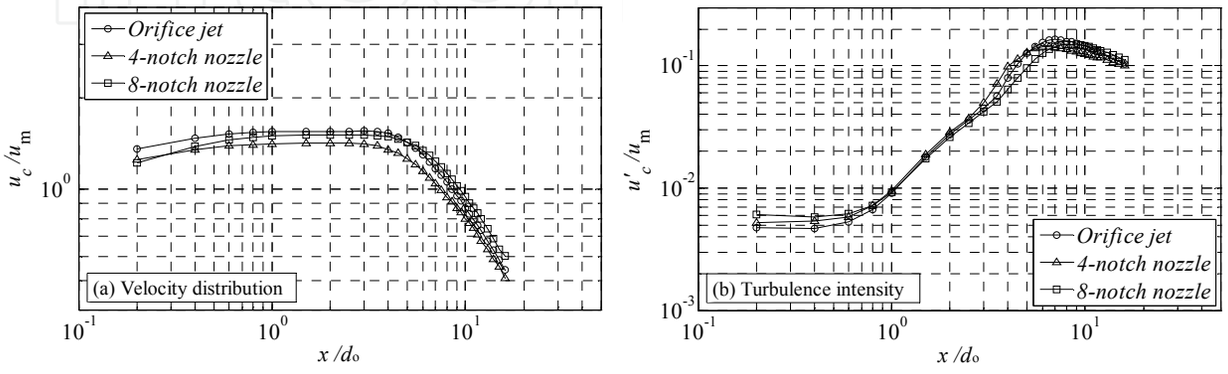

Figure 18. Mean and fluctuating velocity distributions along the jet centerline

4.2.1. Velocity profile and turbulence intensity distribution

Figure 19 (a) and (b) show the cross-sectional mean velocity u/u_m and turbulence intensity u'/u_m for the four-notched jet in the A-A′ and B-B′ directions under the same operation power, respectively. Because the profiles were axisymmetric, only half of the jet is shown in the figure. As mentioned, the nozzle configuration strongly influences the velocity profile at the nozzle exit and the influence can be seen in the downstream region up to $x/d_o = 7$. The jet width in the A-A′ plane is larger than that in the B-B′ plane at the nozzle exit $x/d_o = 0.2$, whereas it decreases at $x/d_o = 2$, which indicates an axis-switching phenomenon. The different development of the mixing layer in the process of jet spreading is observed between the A-A′ and B-B′ planes.

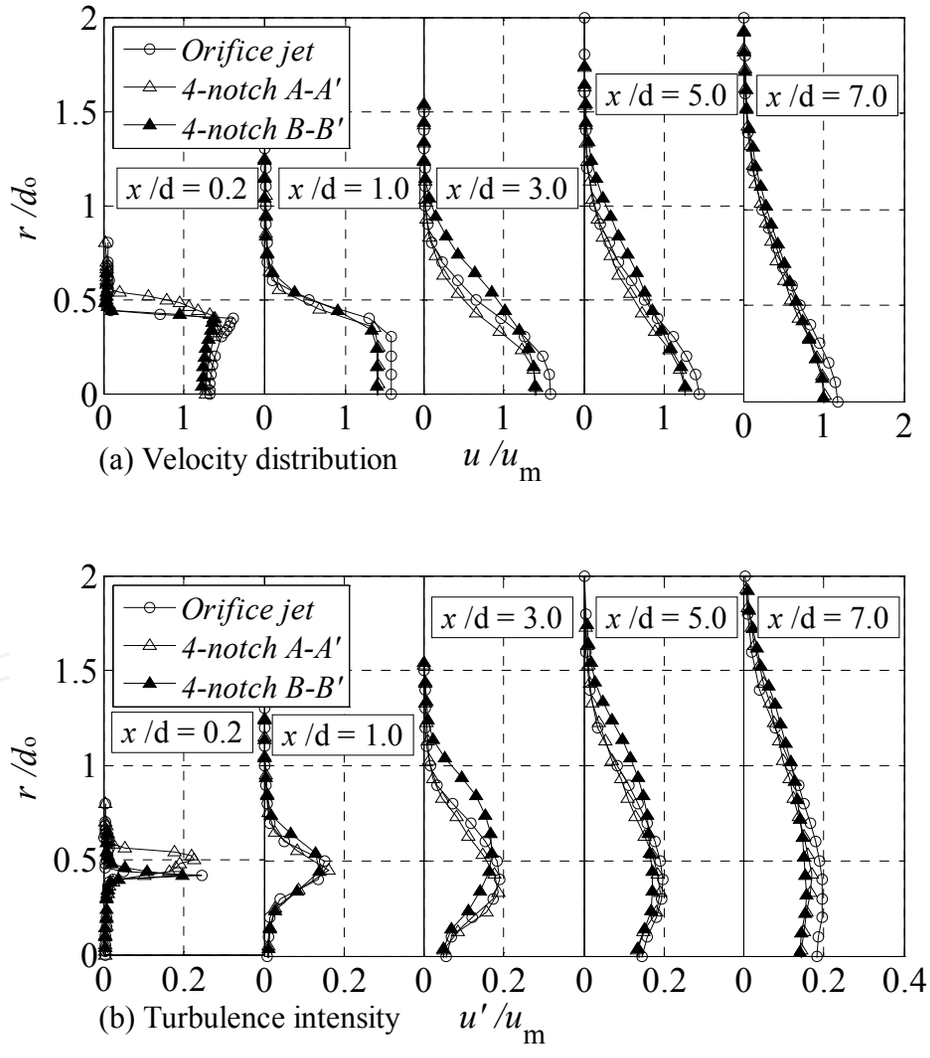

Figure 19. Centerline mean and fluctuating velocities for 4-notched orifice jet

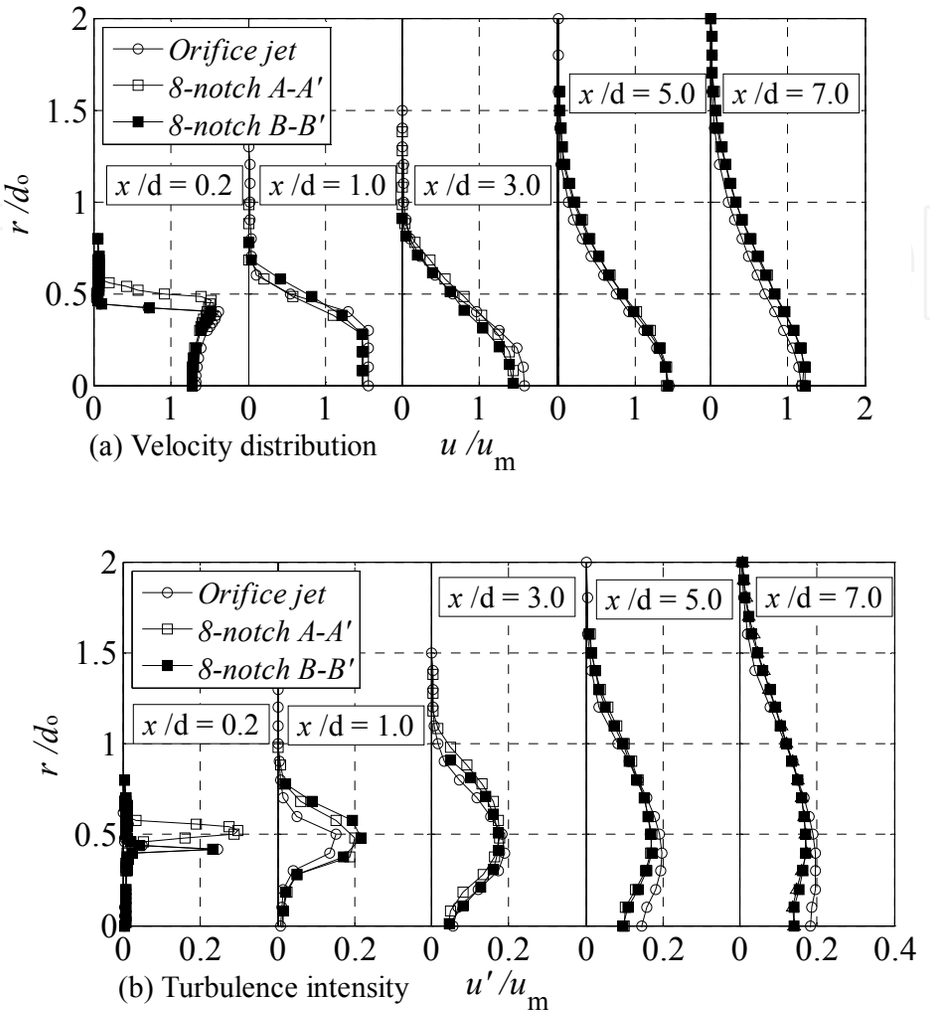

Figure 20. Centerline mean and fluctuating velocities for 8-notched orifice jet

Jets issuing from the eight-notched nozzle, which has a small spacing between the notches spread rapidly because of their instability in the mixing layer, as shown in Fig. 20 (a). The velocity profile in the A-A′ plane similarly coincides with that in the B-B′ plane at $x/d_o = 7$. The velocity profiles in the A-A′ and B-B′ planes at $x/d_o = 2$ are similar and larger than that of the orifice jet at $0.3 < r/d_o < 1.0$. Figure 20 (b) shows that the eight-notched jet flow in the A-A′ plane has high turbulence intensity at the nozzle exit, whereas the orifice jet has high turbulence intensity in the downstream region. This is attributed to the remarkable vena contracta effect and the large velocity gradient at the edge of the jet at $x/d_o = 2$ in the orifice jet flow shown in Fig. 20 (a), except at $0.5 < r/d_o < 1.0$, where the turbulence intensities of the eight-notched orifice jet both in the A-A′ and B-B′ planes are higher than that of the orifice jet.

The high jet velocity and turbulence intensity of the eight-notched jet at $x/d_o = 2$ may improve the heat transfer characteristics more than those of the orifice jets do.

4.2.2. Flow spreading, switching phenomena

Figure 21 shows the jet width b/d_o of the orifice and notched jets under the same operation power. The jet width b was determined from the spanwise location r where the velocity was $u/u_{cm} = 0.1$. The jet width for both notched jets is larger than that for the orifice jet not only because of the larger nozzle exit width with notches but also because of the higher mixing performance with ambient fluid due to an axis-switching phenomenon, which can be seen at $0.2 < r/d_o < 2.0$.

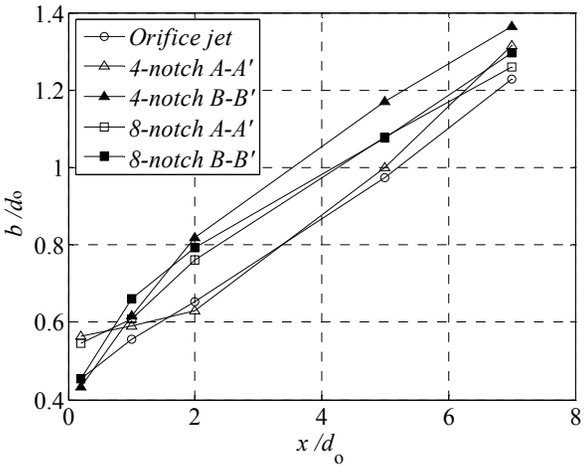

Figure 21. Jet width of the orifice and notched jets under the same operation power

Figures 22 and 23 show equivelocity profiles of the half jet width for four- and eight-notched orifice jets, respectively, that clearly show the axis-switching phenomenon. The notches are located on the axes in Fig. 15.

The pointed parts of the equivelocity profile at the nozzle exit are flattened at $x = d_o$ and the other parts protrude, as indicated by arrows in Fig. 22. The axis-switching phenomenon may be caused by longitudinal vortex flows produced at the edge of the notches. The jet flow entrains ambient flow, which causes the jet to accelerate and decelerate, distorting the vortex ring.

The axis-switching phenomenon, in which a major and minor axis switch to become the minor and major axis, respectively, in the downstream region, is well known in jet flows issued from elliptical or rectangular nozzles with various aspect ratios and cross-shaped nozzles. However, it is not well known that axis switching occurs in notched-orifice jets. We have demonstrated that an axis-switching phenomenon occurs in notched-orifice jets, although the notches are relatively small. Flows issuing from the orifice and notched-orifice nozzles at $Re = 1.0 \times 10^3$ were visualized to demonstrate the effects of the notches on the flow characteristics. Visualized flow patterns of the orifice and notched-orifice free jets using a laser-sheet technique are shown in Figs. 24 and 25, respectively. Figure 24 shows jets at a certain period in the same manner as in Fig. 12. There is no clear vortex in the pipe flow shown in Fig. 24 (a), suggesting the stability of the thick shear layer. In contrast, considerably large coherent vortexes were observed in Fig. 24 (b)–(f), although they were not clear in Fig. 24 (e) and (f) because of the

earlier disintegration of the eight-notched orifice jet. In the case of the standard orifice jet, ring-shaped vortex formations in the shear layer of the jet can be clearly seen in Fig. 24 (b). The discharged ring vortices decayed in the velocity downstream, merging into a large vortex and then disintegrating. Figure 24 (c) and (e) show flow patterns of four- and eight-notched orifice jets, respectively, which were photographed in the middle of the A-A′ plane shown in Fig. 15. The flow patterns in the middle of the B-B′ plane are shown in Fig. 24 (d) and (f). The vortex shedding frequency of four- and eight-notched orifice jets was higher and lower, respectively, than that of the orifice jet. The jets directly issuing from notches such as those shown in Fig. 24 (c) and (e) spread earlier and wider than those in the B-B′ plane because of the high turbulent intensity, although those in the case of the eight-notched orifice jets are not clear because the clearance between the notches is not sufficient to indicate the difference between both planes. The comparison between flows in the A-A′ and B-B′ planes shows a slight difference between the jet widths at the nozzle exit; therefore, the jet width in the B-B′ plane narrower in the A-A′ plane represents high turbulence intensity at the nozzle exit, whereas the orifice jet represents high turbulence intensity in the downstream region. This is attributed to the remarkable vena contracta effect and large velocity gradient at the edge of the jet at $x/d_o = 2$ in the orifice jet flow shown in Fig. 20 (a), except at $0.5 < r/d_o < 1.0$, where the turbulence intensities of the eight-notched orifice jet in both the A-A′ and B-B′ planes are higher than that of the orifice jet. The high jet velocity and turbulence intensity of the eight-notched jet at $x/d_o = 2$ may improve the heat transfer characteristics more than do the orifice jets.

Figure 25(a) is photographs of the impinging pipe jet (CR=1.00). The four small outer holes in the images did not affect the flow since they were screw holes to fix the plate. The jet emitted from the pipe nozzle impinged on the plate with insignificant fluctuations and radically spread producing a thin film on the plate. No large vortex structures or fluctuations could be seen. Ring-shaped flow patterns were, however, observed at $r/d_o \cong 7$, indicating a transition from laminar to turbulent flow. Figure 25 (b) shows the standard orifice impinging jet flow pattern. In the case of the orifice impinging jet, the flow fluctuates at the nozzle edge and spreads radially to produce ring-shaped flow patterns that intermittently impinge on the plate, indicating a transition from laminar to turbulent flow. The interval between ring-shaped patterns corresponds to the vortex-shedding frequency. It is noteworthy that longitudinal vortex structures were observed around the ring-shaped flow patterns. Figure 25 (c) and (d) show flow patterns of four- and eight-notched orifice jets, respectively. The A-A′ and B-B′ planes defined in Fig. 15 are shown in Fig. 25 (c) and (d), respectively. It is clearly observed that the presence of notches strongly affects the flow patterns. The fluctuations at the nozzle edge produce large vortex structures in the downstream region that intermittently impinge on the plate, as observed in the orifice impinging jet. However, the large vortex structures of the notched-orifice jets are distorted by small notches. Diamond-shaped and eight-pointed-star patterns are seen in Fig. 25 (c) and (d), respectively, corresponding to the number of small notches located at the orifice nozzle exit. The fluctuations of the large vortex structure shown in Fig. 25 (c) are higher than those of the structure shown in Fig. 25 (d), indicating that the four-notched orifice nozzle has a high turbulence intensity. This result is consistent with that shown in Fig. 18.

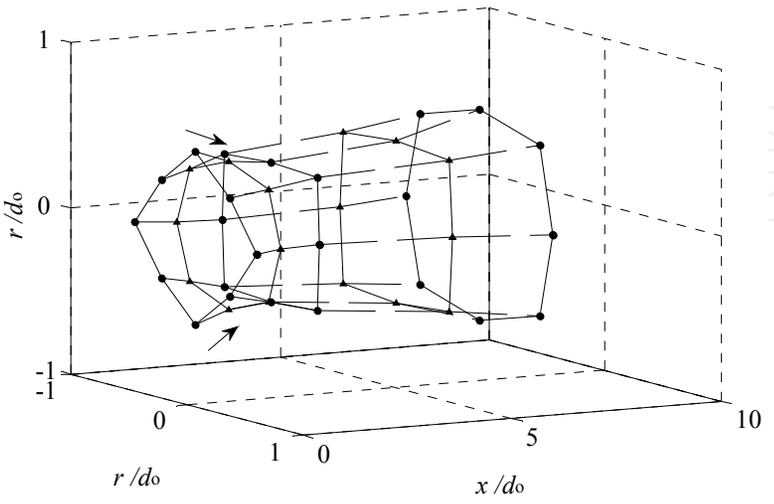

Figure 22. Equi-velocity profile of half width for 4-notched orifice jet

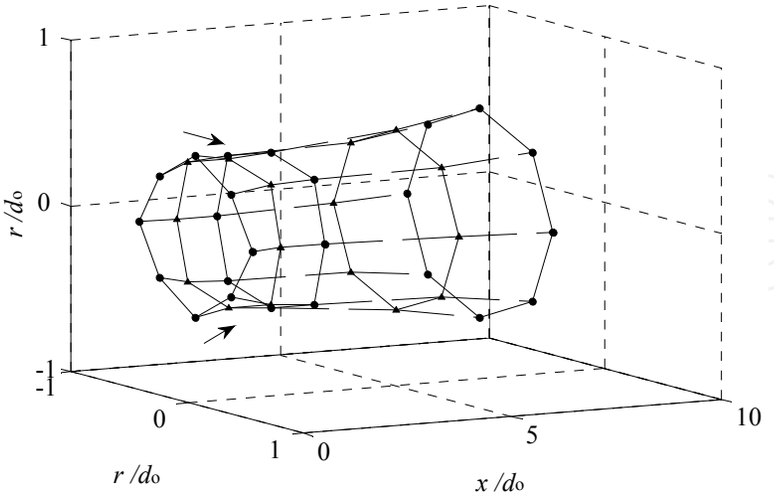

Figure 23. Equi-velocity profile of half width for 8-notched orifice jet

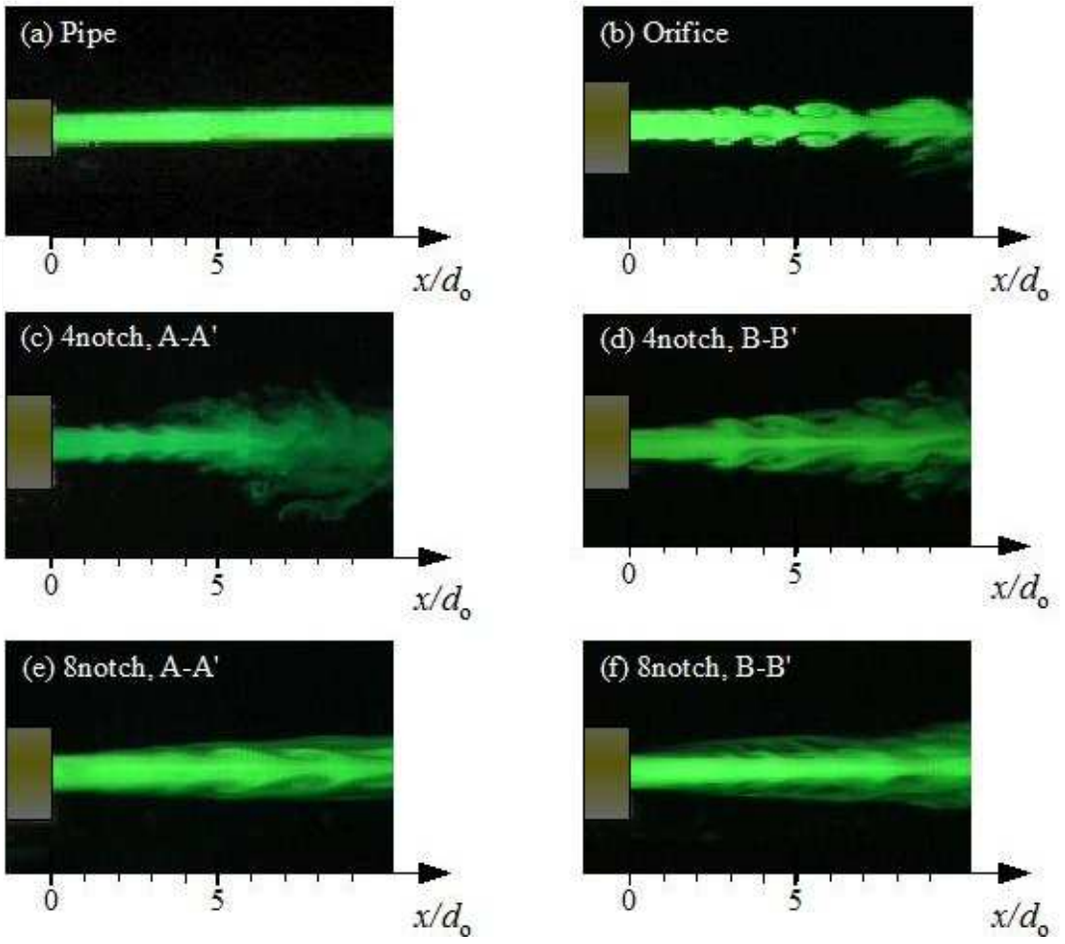

Figure 24. Flow visualization at Re=1.0×10^3

4.3. Heat transfer characteristics

Figures 26 shows the local Nusselt number distribution on the impingement plate at H/d_o = 2.0 under the same operation power. Because of the axisymmetry of the profile, only half the radial distribution from the stagnation point is plotted. The local Nusselt number reaches its maximum near the stagnation point and decreases in the outward direction. The local Nusselt number distribution of the notched-orifice jet is larger than that of the orifice jet in the downstream region because of the larger turbulence intensity caused by the notches.

4.4. Heat transfer enhancement of notched-orifice jet

We discussed the flow and heat transfer characteristics of notched-orifice jets in the previous section and demonstrated that placing notches on the edge of the orifice nozzle can reduce the flow resistance and increase the turbulent intensity. Therefore, the heat transfer performance improved with the use of a notched-orifice nozzle.

In this section, we propose a notched-orifice nozzle that is conically tapered on the inside and investigate the effects of the notches and tapering angle α on the flow and heat transfer characteristics of the proposed orifice jet.

A schematic diagram of the nozzle geometry is shown in Fig. 27. An orifice nozzle with a 10.0-mm exit diameter and a pipe with a 29.75-mm inner diameter [$CR = (d_o/d_i)^2 = 0.27$, see Fig. 27 (a)] was used unless otherwise stated.

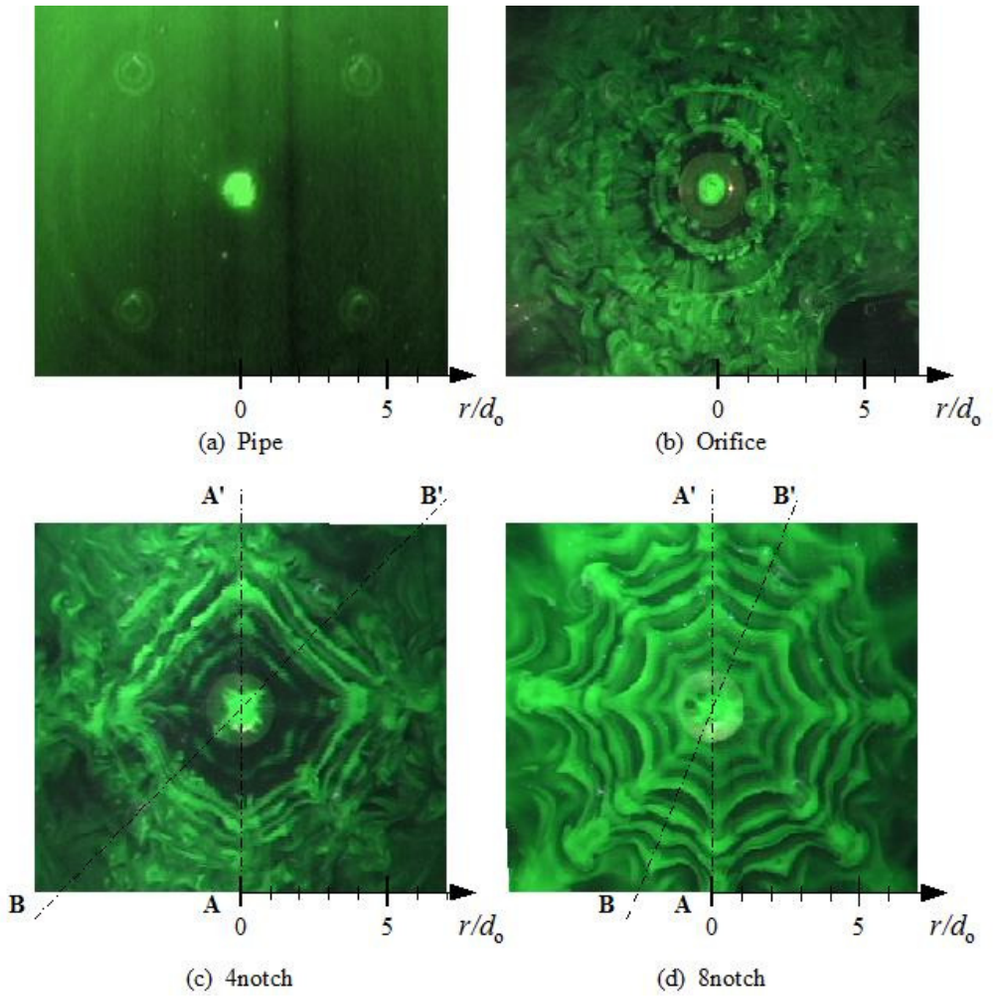

Figure 25. Flow visualization at Re=1.0×10³

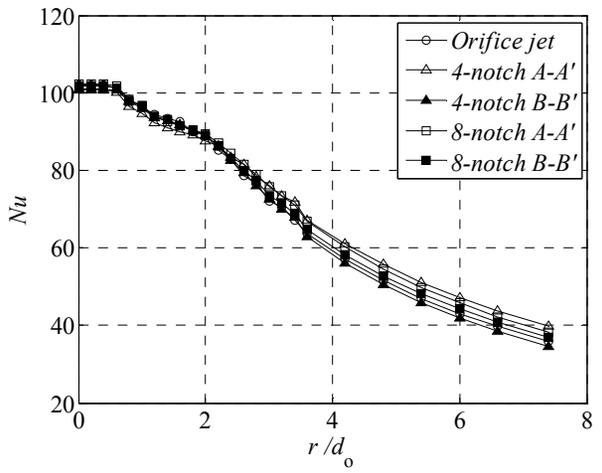

Figure 26. Local Nusselt number (H/d_o=2.0)

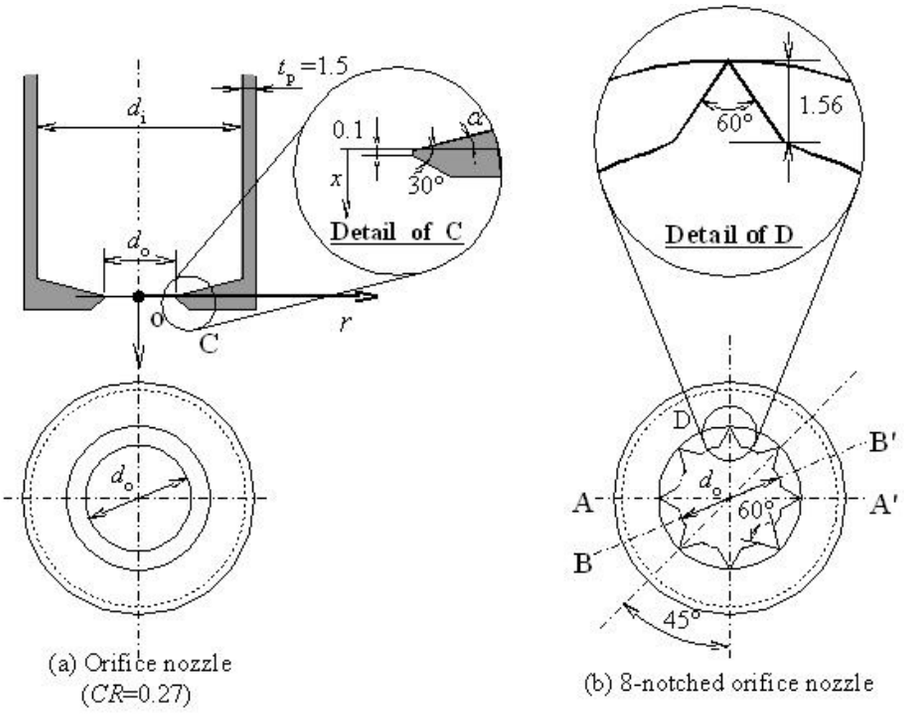

Figure 27. Nozzle configuration

Figure 27 (b) shows an orifice nozzle with eight notches having 60° openings and 1.56-mm depths. The inside of the eight-notched orifice nozzle is conically tapered at angles of $\alpha = 0°$, 5°, 10°, and 15°. A pipe nozzle with a 10-mm inner diameter was also used for comparison. Every nozzle was 500-mm long and 1.5-mm thick.

Figure 28 shows the flow rate improvement rate, $(Q - Q_0)/Q_0$, for orifice jets that are conically tapered on the inside as compared to the orifice jet without notches at the nozzle exit under the same operating power. The flow rate Q of the notched-orifice jet increases while the flow resistance decreases compared to that of the orifice jet without notches because of the increase in the cross-sectional area at the nozzle exit.

The flow rate of notched-orifice jets Q increases linearly with the tapering angle α. Q of eight-notched orifice jets with $\alpha = 0°$, 5°, 10°, and 15° increased by 10.9%, 11.3%, 13.1%, and 13.5% respectively, compared with that of the orifice jet.

Figure 29 shows the mean and fluctuating velocity distributions in the A-A′ direction at the nozzle exit $x/d_o = 0.2$ for notched-orifice jets. The mean exit velocity u/u_m is plotted on the left-hand side of Fig. 29 and the fluctuating velocity u'/u_m is plotted on the right-hand side because they were, respectively, axisymmetric. The results in the B-B′ direction at the nozzle exit are plotted in Fig. 30 in the same manner.

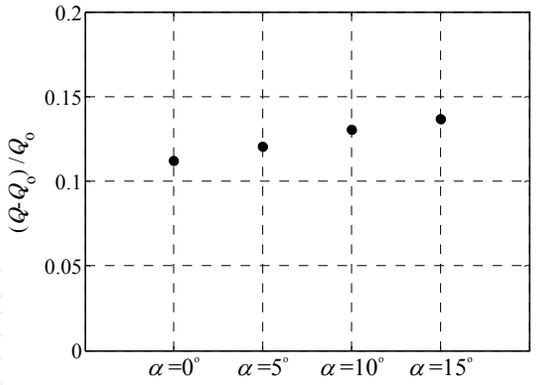

Figure 28. Increment rate of flow rate of notched-orifice nozzle to orifice nozzle

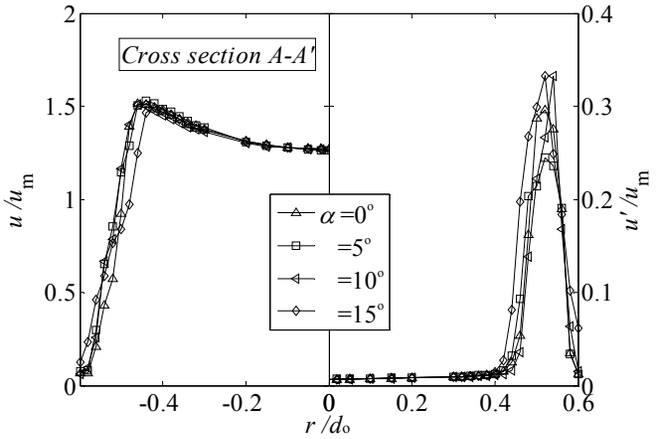

Figure 29. Mean and fluctuating velocities at the nozzle exit (x/d_o=0.2) in the A-A' plane

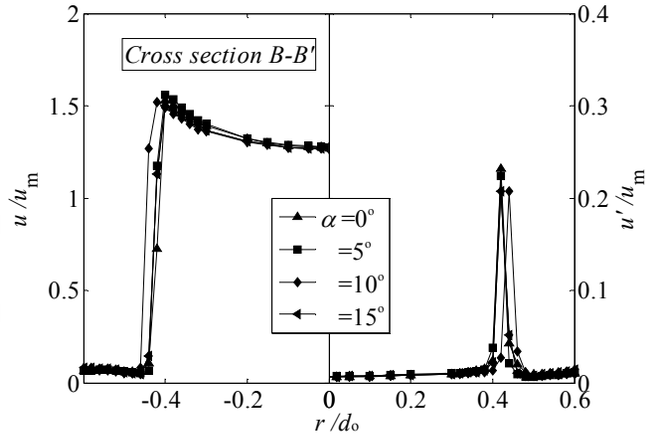

Figure 30. Mean and fluctuating velocities at the nozzle exit (x/d_o=0.2) in the B-B' plane

A similar profile can be seen for the notched-orifice jets, especially in Fig. 30. The jet widths of the notched-orifice jets increase because of the notches in the A-A′ plane, whereas the vena contracta effects appear in the B-B′ plane. The maximum velocity occurs at r/d_o = 0.45, which is smaller than the nozzle edge due to the vortex generated by the notches. The fluctuating velocity of the notched-orifice jets increases in the A-A′ plane.

The fluctuating velocity reflecting the steep velocity gradient near the center of the jet is higher than that of the notched-orifice jets that are discharged toward the center of the jet and accelerated. The turbulence intensity near the nozzle exit is larger than that of the other jets because the pipe jet has a fully developed turbulent velocity profile; however, the growth of the turbulence intensity is gradual and the turbulence intensity decreases at $x/d_o \geq 3$.

The heat transfer characteristics of the orifice and the notched-orifice impinging jets with tapering under the same operating power are shown in Fig. 31. The enhanced Nu number of the notched-orifice jets with tapering is observed in the downstream region due to the high turbulence intensity caused by the notches. However, in the case of the orifice jet, the heat transfer coefficients decrease more than in the case of the others in the downstream region because of the size of the nozzle exit.

Figure 32 shows the increasing ratio of the mean Nu number Nu_m in relation to that of the orifice jet for notched-orifice jets with tapering angle α under the same operating power. Nu_m was obtained by averaging the mean Nu number in the A-A′ and B-B′ directions considering the measured temperature as the reference temperature in the range of $\alpha = 2\pi/16$ [rad]. The mean Nu number for the notched-orifice jet has almost the same value at $r/d_o \approx 2$ as that of the orifice jet. The ratios of Nu_m of the notched-orifice jets with tapering in the downstream region $r/d_o > 3.3$ were larger than that of the orifice jet. The heat transfer for a notched-orifice jet with $\alpha = 10°$ increases by a maximum of ~4.5% in the downstream region. In addition, the increasing ratio of Nu_m to that of the pipe jet under the same operating power was also calculated. The ratio of Nu_m to that of the pipe jet was attained at $\alpha = 0°$ and reached a maximum of 6.7% and the heat transfer characteristics for $\alpha = 0°$, 5°, 10°, and 15° were enhanced by ~3.4%, 3.7%, 4.6%, and 4.5%, respectively, in the downstream region at $r/d_o = 7.4$.

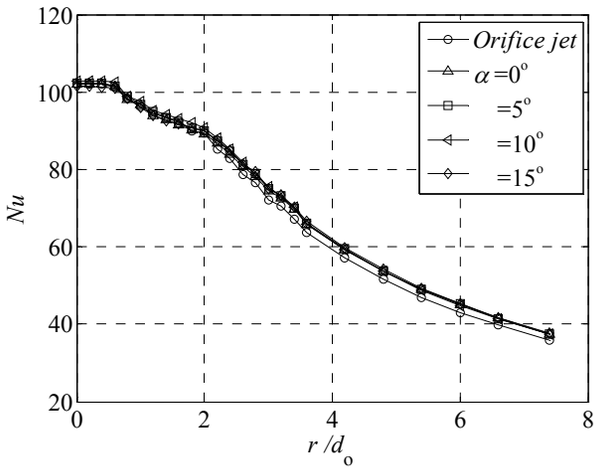

Figure 31. Local Nusselt number (H/d_o=2.0)

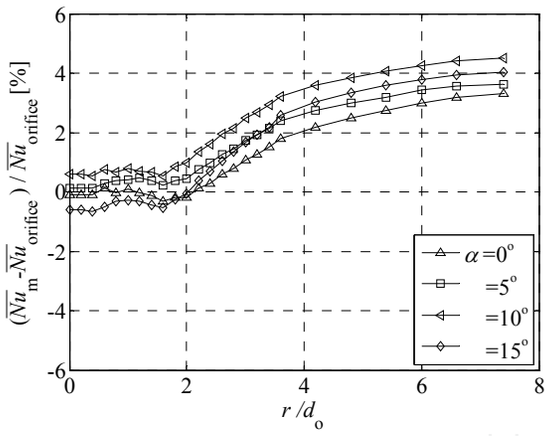

Figure 32. Increasing ratio of average Nu_m to the orifice jet (CR=0.27)

5. Conclusion

In this chapter, the reviews of the impingement heat transfer of various types of jets were introduced in brief, and then, the flow and impingement heat transfer of orifice jets were examined in detail. In particular, the effects of the nozzle contraction area ratio CR on the flow and heat transfer characteristics of the jet issuing from an orifice nozzle were examined experimentally and visually. The following conclusions were obtained.

1. CR was found to strongly depend on the large vortex structures of a submerged orifice water jet in visualized images. A more coherent vortex was produced with a decrease in CR. Smaller CR strongly promoted mixing with the ambient fluid and widened the jet spreading.
2. The dimensionless centerline maximum velocity u_c/u_m can be expressed as

$$u_c / u_m = 1.9CR^3 - 3.55CR^2 + 1.38CR + 1.53 ,$$

which has a maximum value of 1.7 at CR = 0.27.

Velocity vectors toward the centerline at the orifice nozzle exit that were produced by the contraction contributed to the increase in the centerline velocity, which was maximum for CR = 0.27.

Next, in order to simultaneously reduce the flow resistance, increase the turbulent intensity, and obtain the vena contracta effect, we proposed a notched-orifice nozzle. The effects of notches at the orifice nozzle exit edge on the flow and heat transfer characteristics were investigated. Moreover, we proposed notched-orifice nozzles with tapering to reduce the resistance further. The proposed tapering angle has also been taken into consideration, resulting in the following conclusions.

i. Small notches greatly affect the flow structure of jets and reduce the nozzle resistance or operating power as well as increase turbulence at the nozzle exit. The local Nusselt number distribution of the notched-orifice jet is larger than that of the orifice jet in the downstream region because of the larger turbulence intensity caused by the notches.

The turbulence intensity of the four-notched orifice jet increases along the centerline by ~47.2% at $x/d_o = 3.5$ compared with the other jets under the same operating power.

ii. Axis-switching phenomena occur in the notched-orifice jets, although the notches are relatively small.

iii. The heat transfer characteristics of the eight-notched orifice jet with a tapering angle of $\alpha = 10°$ were a maximum of 6.7% greater than those of the pipe jet at $r/d_o = 2.2$ and were greater in the downstream region compared to the orifice jet.

Nomenclature

A_i: Cross –sectional area of pipe [m^2]
A_o: Nozzle exit area [m^2]
b: Jet width where the velocity ratio $u/u_c = 0.1$ [m]
$b_{1/2}$: Half jet width [m]
CR: Contraction area ratio (=A_o/Ai)
d_i: Diameter of pipe [m]
d_o: Diameter of nozzle exit [m]
f: Frequency [Hz]
f^*: Normalized frequency (= $f\, d_o/u_c$)
H: Nozzle – plate distance [m]
h: Heat transfer coefficient [W/(m^2·K)]
Nu: Local Nusselt number (= $h\, d_o/\lambda_a$)
$\overline{Nu}$: Mean Nusselt number
$\overline{Nu}_m$: $\overline{Nu}$ obtained approximately by summing and averaging Nu calculated from the temperature distribution in the A-A′ and B-B′ directions considering the measured temperature as the reference temperature in the range of $\theta = 2\pi/16$ [rad.]
Q: Flow rate [m^3/s]
r: Spanwise distance from the center of nozzle [m]
p_a: Atmospheric pressure [Pa]
Re: Reynolds number (= $u_m\, d_o/\nu$)
u: Mean velocity [m/s]
u_c: Mean velocity along the centerline [m/s]
u_m: Mean velocity at the nozzle exit [m/s]
u_{max}: Maximum velocity [m/s]
u_{pm}: Mean velocity in the pipe [m/s]
u': Fluctuating velocity [m/s]
W: Operation power based on the pressure loss at the nozzle exit [W]
x: Streamline distance from the nozzle exit [m]
α: Taper angle of the nozzle plate
Δp: Pressure loss at the nozzle [Pa]
ρ: Air density [kg/m^3]
ν: Coefficient of kinematic viscosity [m^2/s]

λ_a: Air thermal conductivity [W/m·K]
ν: Kinetic viscosity [Pa·s]
Φ_y': Normalized power spectra density function

Author details

Toshihiko Shakouchi and Mizuki Kito
Graduate School of Engineering, Mie University/Suzuka National College of Technology, Japan

6. References

Antonia, R. A. & Zhao, Q. (2001). Effect of Initial Conditions on a Circular Jet, *Experiments in Fluids,* Vol.31, No.3, (September 2001), pp. 319-323, ISSN 0723-4864

Downs, S.J. & James, E.H. (1987). Jet Impingement Heat Transfer – A Literature Survey, *ASME National Heat Transfer Conference,* No.87-H-35, ASME, New York

Hrycak, P. (1981). Heat Transfer from Impinging Jets: A Literature Review, *AWAL*-TR-81-3054

Kataoka,K., Suguro,M., Degawa,H., Maruo,K. & Mihata,I. (1987). Effect of Surface Renewal Due to Large-Scale Eddies on Jet Impingement Heat Transfer, *International Journal of Heat and Mass Transfer*, Vol.30, pp.559-567, ISSN 0017-9310

Lee, J. & Lee, SJ. (2000). The effect of nozzle configuration on stagnation region heat transfer enhancement of axisymmetric jet impingement, *International Jouranal of Heat and Mass Transfer,* Vol.43, No. 18, (September 2000), pp. 3497-3509, ISSN 0017-9310

Livingood, J.N.B. & Hrycak, P. (1973). Impingement Heat Transfer from Turbulent Air Stream Jets to Flat Plates – A Literature Survey, *NASA* TM X-2778

Martin, H. (1977). *Heat and mass transfer between impinging gas jets and solid surface*, In: *Advances in Heat Transfer,* Hartnett, J.P. & Irvine, T.F. (Eds), 1-60, Vol.13, ISBN 0-12-020013-9, Academic press, New York

Mi, J., Nathan, G.J. & Nobes, D.S. (2001). Mixing Characteristics of Axisymmetric Free Jets from Contoured Nozzle, an Orifice Plate and a Pipe, *Jouranal of Fluids Enginerring-Transactions of the American Society of Mechanical Engineers,* Vol.123, No.4, (December 2001), pp. 878-883, ISSN 0098-2202

Quinn, W R. (2006). Upstream nozzle shaping effects on near field flow in round turbulent free jets. *European Journal of Mechanics B/ Fluids,* Vol.25, No.3, (May 2006), pp. 279-301, ISSN 0997-7546

Shakouchi, T. (2004). *Jet Flow Engineering –Fundamentals and Application–,* Morikita, ISBN 978-4-627-67201-7, Tokyo, Japan

Viskanta, R. (1993). Heat Transfer to Impinging Isothermal Gas and Flame Jets, *Experimental Thermanl and Fluid Science,* Vol.6, No. 2, (February 1993), pp. 111-134, ISSN 0894-1777

Yokobori, S., Kasagi, N., Hirata, M & Nishiwaki, N. (1978). Role of Large-Scale Eddy Structure on Enhancement of Heat Transfer in Stagnation Region of Two-Dimensional, Submerged, Impinging Jet, *Proceedings of 6th International Heat Transfer Conference,* pp.305-310, Toronto, Canada, August 1978

Zhou,D.W, Lee,S.J., Ma,C.F. & Bergles, A.E. (2006). Optimization of mesh screen for enhancing jet impingement heat transfer, *Heat and Mass Transfer,* Vol.42, No. 6, (February 2006), pp. 501-510, ISSN 0947-7411